

The Solar Neighborhood: Habitable Real Estate around Nearby Stars

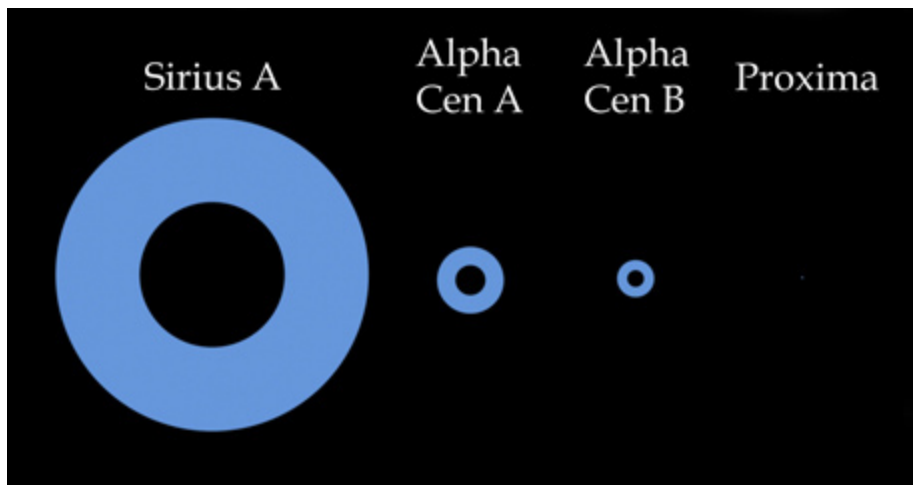
Justin Cantrell & Todd Henry (Georgia State University)

Early astronomers looked to the Moon and saw a habitable world covered in vast oceans. Venus was once thought to be a swampy marshland enshrouded in clouds. Mars had grand canals built by advanced beings. Alas, none of these worlds has maintained their promise of rich life. Instead, the Solar System, once thought to be teeming with life, may be barren, although hope remains for environments under the icy crust of Europa, in the tiger stripes of Enceladus, under the Martian surface, or lurking somewhere as yet unidentified.

However, with the discovery of more than 200 extrasolar planets since 1995, the real estate market in our Solar System is no longer the only place we might look for evidence of life beyond Earth. Perhaps moons circling the gas giant planets found in stars' habitable zones could harbor life. Among the smaller and presumably solid-surfaced planets detected, only one world orbiting Gliese 581 may be in the habitable zone.

The term "habitable zone" (HZ) was first coined by Huang in 1959 as a region around a star where a planet could support life. Since then, there have been many definitions of habitability, most based on the presence of liquid water on the surface of a planet. The continuously habitable zone (CHZ) was introduced to put a temporal restraint on the habitability of a star.

To investigate the market in the solar neighborhood, we have determined the amount of habitable "real estate" for 62 stars nearer than 5 parsecs (pc). In defining our HZ requirements, we use an "Earth-like" model, assuming planets with atmospheres, radii, and albedos matching that of Earth. We define the HZ to be where liquid water is present at the present time (we do not include a continuously habitable zone). Following the work of Kasting et al. (1993), the inner boundary of our HZ is marked by the loss of water via photolysis and hydrogen escape, while the outer boundary of our HZ is set by the formation of CO₂ clouds that cool a planet's surface by increasing its albedo and lowering its convective lapse rate. The resulting



The relative sizes of traditional habitable zones are shown around four of the nearest stars. Sirius A is the brightest star in the night sky, while Alpha Centauri AB, and Proxima Centauri are three stars forming the nearest star system, which is a triple. At this scale, the habitable zone around the red dwarf Proxima is so small that it is only about the size of the period at the end of this sentence.

inner and outer radii of the HZ correspond to temperatures of 285 K to 191 K, respectively. These values are based on empirical evidence that Venus has not had water for at least one billion years, and Mars may have been habitable around 3.8 billion years ago. These temperatures were chosen based on the effective temperature of an Earth-like planet that would lie just outside the orbit of Venus all the way out to the orbit of Mars. We then utilized the habitable zone equation from Kaltenegger et al. (2002) to find the inner and outer radii of the HZ for each star.

Similar to previous efforts, our first goal was to evaluate the HZ real estate for individual nearby stars, which is set by a combination of stellar temperatures and radii, and the distance of our Earth twin from a given star. We used photometric spectral energy distributions (SEDs) derived using available and new UVRIJHK photometry from observations by the Research Consortium on Nearby Stars (RECONS) made at the CTIO 0.9-m and 1.5-m telescopes. For stars with radii measured via long-baseline interferometry, the radius was fixed and only the temperature was allowed to vary. We fit the photom-

etry to GAIA models, which in most cases adequately address the significant offsets from blackbody emissions found in real stars, especially for the red dwarfs. In nearly every case, we were able to recover radii within 10% of the measured interferometric radii (when available), thereby allowing us to be confident that the derived temperatures and radii are reliable.

Our second goal is new—to compare the aggregate HZ real estate for each spectral type of star in the solar neighborhood. RECONS is in an ideal position to carry out this comparison, as our group uses the CTIO 0.9-m to measure trigonometric parallaxes for previously unknown nearby stars (Henry et al. 2006), and we keep track of the resulting nearby stellar census. Results indicate that although there is only one A spectral type and one F spectral type within 5 parsecs, their wide HZs provide significantly more real estate that is good for life than the more numerous but smaller parcels available around 44 M dwarfs. However, this calculation has been done using HZ areas, which is likely not the best measuring technique for HZs. Considering that planets are spaced logarithmically in

continued

The Solar Neighborhood continued

the solar systems found to date (i.e., planets cannot be found every 0.1 AU between the orbit of Venus and Mars in our Solar System, and two planets are not likely to be found in the same orbit), using HZ areas is likely less reliable than measuring real estate by linear AU. When doing so, the 44 M dwarfs en masse provide 3.3 linear AU of distance for habitable planets compared to 4.6 linear AU for A stars and 1.7 for G stars like the Sun.

We also are mapping out the HZ real estate in multiple star systems to see if a planet with two suns in its sky has a fair chance of remaining habitable. Good real estate was mapped out for a few noteworthy binaries at their most extreme moments—when a companion star was at perihelion to a planet in

orbit around the star of interest. It turns out that for systems such as the G dwarf/K dwarf pair of Alpha Centauri AB and the double M dwarf of Gliese 65 AB, the shift in HZ inner and outer radii is less than 1%. Thus, habitable worlds could exist comfortably in many different types of stellar systems.

The table below lists the number of stars that were studied, by spectral type, within 5 pc. Shown are the number of stars per spectral type, the total habitable zone listed by area, and the linear Astronomical Units (AU) of habitable zone per spectral type. Taken together, these stars offer a vast 251 square AU of habitable real estate available for potential development by enterprising life-forms among our nearest neighbors. ☼

Cumulative Habitable Zones for Stars within Five Parsecs

SpType	#Stars	HZ Areas (AU ²)	HZ Linear (AU)
A	1	177	4.6
F	1	49	2.4
G	2*	13	1.7
K	6	9	2.5
M	44	3	3.3

* Not including our Sun

Lyman-Alpha Emitting Galaxies at $z = 3.1$: Progenitors of Present-Day L^* Galaxies

Eric Gawiser (Rutgers), Caryl Gronwall & Robin Ciardullo (Penn State), John Feldmeier (Youngstown State), & the MUSYC Collaboration

A multi-observatory, multi-wavelength study that began on the Blanco 4-m telescope at CTIO has produced the exciting result that Lyman-alpha emitting (LAE) galaxies at redshift 3.1 are the first high-redshift objects to be identified as the precursors of typical present-day galaxies.

Lyman-Alpha Emitters at $z = 3.1$

Our collaboration was forged after the NOAO Time Allocation Committee (TAC) pointed out that we were engaged in duplicate efforts to image the Extended Chandra Deep Field-South (ECDF-S) through a narrow-band filter of 5,000 Å. We then used a combination of US and Chilean observing time on the Mosaic II camera of the Blanco 4-m telescope at CTIO to obtain a deep (20-hour) exposure of the 31'x31' ECDF-S. Our narrow-band imaging was used to select a sample of 162 LAEs at $z = 3.1$ with emission line fluxes $>1.5 \times 10^{-17}$ ergs $\text{cm}^{-2} \text{s}^{-1}$ and observed-frame equivalent widths >80 Å. We measured the continuum and emission-line luminosity functions and found that the LAEs have a median continuum magnitude of $M_r = 27$ and very blue continuum colors similar to those of Lyman-break galaxies (Gronwall et al. 2007, Gawiser et al. 2006b).

Archival Hubble Space Telescope images of the GOODS-South region taken with the Advanced Camera for Surveys show the LAEs to be small (0.5–2 kpc in half-light radii) with many showing clumpy structures. The best-fit Sersic profiles show a range from disk-like to bulge-like. In contrast to modern disks, the disk-like profiles are probably due to clumpy linear structures, in some cases, showing evidence of interaction or merging between multiple small galaxies (see figure 1).

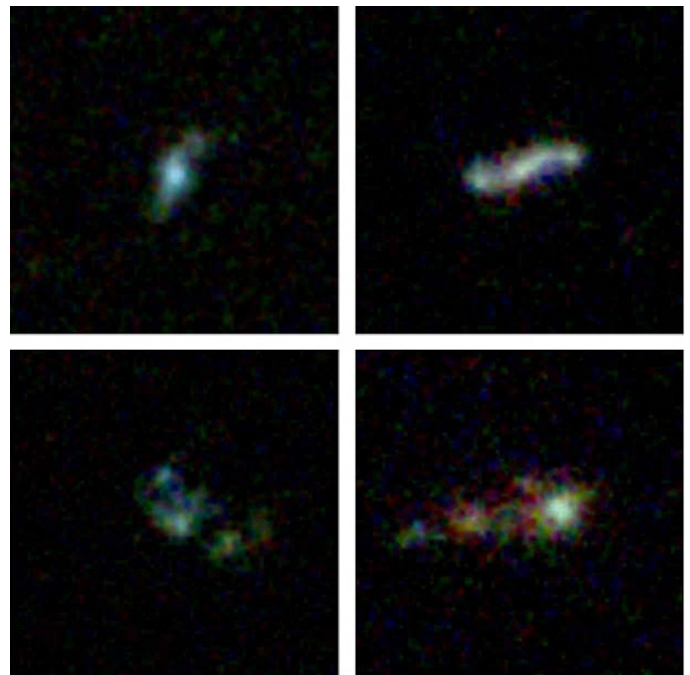


Figure 1: Lyman-alpha emitting galaxies 12 billion light years from Earth, as imaged by the Hubble Space Telescope’s Advanced Camera for Surveys. Credit: NASA, ESA, Caryl Gronwall/Penn State.

continued

Lyman-Alpha Emitting Galaxies continued

Spectroscopic follow-up determined precise redshifts for 60 of these objects at $3.08 < z < 3.13$ and showed no evidence for contamination from lower-redshift emission-line galaxies (Gawiser et al. 2007). Through a combination of NOAO-TSIP and Chilean time, we used the Inamori Magellan Areal Camera and Spectrograph (IMACS) on the Baade telescope at the Las Campanas Observatory at $R \sim 1000$ covering 4,000–9,000 Å. Each IMACS mask contained ~ 100 objects combining a range of MUSYC science projects and was observed for ~ 5 hours in order to reach a magnitude limit of $M_R \sim 23$ in the continuum.

Clustering Analysis

The LAEs exhibit a moderate spatial correlation length of 3.6 Mpc, corresponding to a bias factor of 1.7, meaning that their clustering is 1.7 times stronger than that of the underlying dark matter (Gawiser et al. 2007). This in turn implies a median dark matter halo mass close to $10^{10} M_\odot$. It appears, however, that LAEs only occupy a few percent of the dark matter halos in this mass range, as their observed space density of $1.5 \times 10^{-3} \text{ Mpc}^{-3}$ is significantly less than the space density of dark matter halos in this mass range. The evolution of galaxy bias with redshift, as shown in figure 2, implies that LAEs at $z = 3.1$ evolve into present-day galaxies with $L \sim L^*$ (e.g., figure 3). Other $z > 3$ galaxy populations, including Lyman-break galaxies (LBGs), distant red galaxies, and active galactic nuclei (AGN) evolve into more massive galaxies (e.g., Francke et al. 2008, Quadri et al. 2007a).

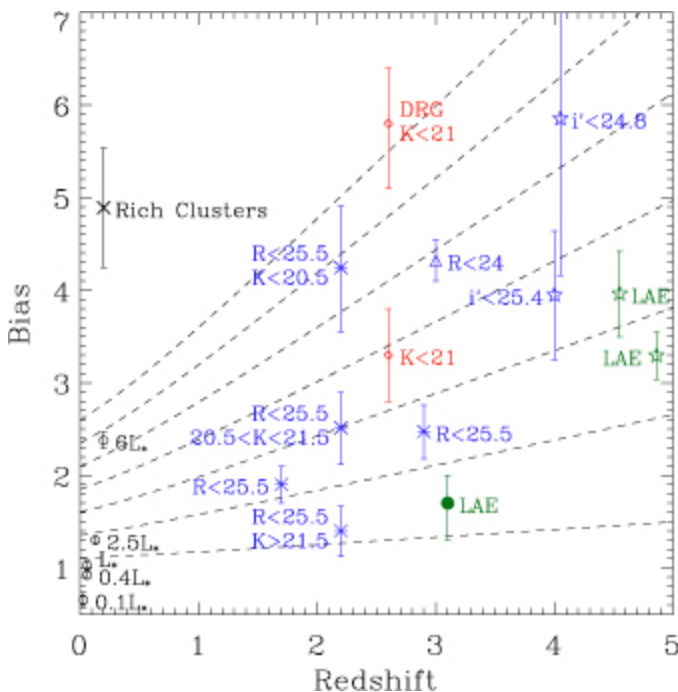


Figure 2: Tracks show the evolution of bias with redshift. The filled circle shows our result for the bias of LAEs at $z = 3.1$. Results from the literature are also shown for LAEs at $z = 4.5$ and $z = 4.86$ (stars); LBGs at $z \sim 4$ (stars); K-selected galaxies (diamonds); bright LBGs at $z \sim 3$ (triangle); and BM, BX, and LB galaxies (asterisks). Local galaxy clustering is shown for SDSS galaxies and for rich clusters. K-band limits are in Vega magnitudes. See Gawiser et al. 2007 for the original figure with complete references.

Star Formation Histories

Information at near-infrared (near-IR) wavelengths is very important as these bands trace the rest-frame optical light at high redshift. The $30' \times 30'$ ECDF-S field was covered up to a magnitude limit of $K \sim 22$ using the Infrared Sideport Imager (ISPI) on the CTIO Blanco 4-m telescope. This detector provides a field of view of $10.5' \times 10.5'$, one of the widest cameras available in the near-IR. Spitzer coverage includes a Cycle 2 Legacy Survey with IRAC (SIMPLE, PI van Dokkum) and MIPS 24-micron and 70-micron imaging from GTO observations (PI Rieke) and FIDEL (PI Dickinson).

Our rich, multi-wavelength data set has yielded significant advances in understanding the nature of LAEs. Only 30% of LAEs have sufficient stellar mass ($> 3 \times 10^9 M_\odot$) to yield detections in deep IRAC images (Lai et al. 2008). Our two-population fit to the stacked spectral energy distribution of the IRAC-undetected LAEs found low stellar mass ($\sim 10^9 M_\odot$), moderate star formation rates ($\sim 2 M_\odot/\text{yr}$), a young component age of ~ 20 Myr, little dust ($A_V < 0.2$), and no evidence for a substantial AGN component (only 3/162 LAEs are detected in X-rays). The lack of ultra-high equivalent-widths in our $z \sim 3$ sample argues that the $z \sim 3$ LAEs do not represent primordial Pop III objects, even though they may be experiencing their first bursts of star formation.

The MUSYC Survey

MUSYC (the Multiwavelength Survey by Yale-Chile, PIs Gawiser and van Dokkum) is unique among the current generation of wide-deep surveys in having been optimized for the study of the high-redshift ($z > 3$) universe. This is achieved by imaging 1.2 square degrees spread over four fields (see figure 4) down to the spectroscopic limit for modern 8-m telescopes with coverage from U-band through K-band to trace both the Lyman and Balmer/4000Å breaks at $z \sim 3$ and prioritizing high-redshift candidates for spectroscopy.



Figure 3: Galaxy M74 (NGC 628) is representative of spiral galaxies that evolved from Lyman-alpha emitting galaxies in the early universe. Credit: Todd Boroson/NOAO/AURA/NSF.

continued

Lyman-Alpha Emitting Galaxies continued


The 1.2-square-degree optical catalog contains 277,341 sources with a 50% completeness limit of $M_R \sim 26.5$. The fields were chosen to have the lowest possible Galactic reddening, HI column density, and dust emission at 100 microns. Additionally, these fields are accessible from Chile, making them a natural choice for follow-up studies with ALMA. The collaboration includes a total of 30 investigators from the US, Chile, and Europe plus six Ph. D. students. Detailed descriptions of the data reduction techniques are presented by Gawiser et al. (2006a), Quadri et al. (2007b), and Blanc et al. (2008). All data from this survey will be made public, with reduced images and catalogs already available from the narrow-band, broad-band optical and near-IR imaging. Instructions for download of the data and more information about the survey can be found at the Web page www.astro.yale.edu/MUSYC. 



Figure 4: Optical images (UBR) of the four 30'×30' fields in the MUSYC survey. Each field was imaged with the CTIO 4-m+Mosaic II, although these images of ECDF-S come from ESO 2.2-m+WFI.

Observation of Alfvén Waves in the Solar Corona

Steve Tomczyk, Scott McIntosh, & Phil Judge (High Altitude Observatory), Stephen Keil (National Solar Observatory), Tom Schad (NSO REU, Notre Dame, now a University of Arizona graduate student), Dan Seeley (NSO RET, Framingham High School), & Justin Edmondson (HAO REU, University of Michigan)

Why the solar corona reaches temperatures of millions of degrees while the solar surface (photosphere) is only a few thousand is a long-standing problem in solar physics. Hannes Alfvén first postulated the existence of oscillations of magnetized plasma in 1942. The Alfvén wave is an incompressible, transverse oscillation, which propagates along field lines, with magnetic tension as the restoring force. Alfvén waves were soon postulated as a possible source of the energy that heats the solar corona (Alfvén 1947, Osterbrock 1961).

To first order, Alfvén waves do not create detectable intensity fluctuations, and thus the imagers used for most coronal observations will not see them. Velocity fluctuations inferred from Doppler shifts of emission lines require spectrograph or narrow-band

filtergraph measurements; most coronal work has been performed with spectrographs that cannot observe over a large enough field of view in a time that is sufficiently short compared to wave periods. Thus, in spite of their importance for coronal heating, definitive observations of Alfvén waves in the coronal plasma have been lacking.

The data used in this study were obtained with the Coronal Multi-channel Polarimeter (CoMP) attached to the Coronal One Shot (COS) coronagraph mounted on the Hilltop spar at Sacramento Peak. CoMP is a combination polarimeter and narrowband tunable filter, which can measure the complete polarization state of coronal emission lines in the near-infrared. Observations consisting of images of the corona between 1.05 and ≈ 1.35 solar radii (R_{sun}) in the four Stokes parameters

(I , Q , U , and V) at three wavelengths across the Fe XIII 1074.7 nm line (red wing, line center, and blue wing) were obtained every 29 seconds on 30 October 2005, between 14:15 UT and 23:33 UT. The spatial sampling was 4.5 arcsec per pixel. The Fe XIII 1074.7 nm line is formed at about 1.6 MK. After removing residual image motion between frames, we computed the velocity and intensity at line center by fitting Gaussians to the three wavelength points at each pixel. We also computed the degree of linear polarization (p) and the azimuthal direction of the magnetic field (ϕ) in the plane of the sky from:

$$p = \sqrt{Q^2 + U^2} / I, \quad \phi = 0.5 \tan^{-1}(U/Q)$$

where ϕ has the well-known ambiguity of 180°, which does not affect our analysis, and a possible 90° ambiguity due to the van

continued

Observations of Alfvén Waves in the Quiet Solar Corona continued

Vleck effect (see, for example, Querfeld, Smartt 1984), which does not appear to have affected very many of our computed azimuths.

The first three panels in figure 1, show maps of mean intensity, velocity, and line width for the part of the corona that we have analyzed. This section of corona contained both active region loops and a coronal cavity. A movie of the velocity images reveals ubiquitous, quasi-periodic fluctuations with a root-mean-square amplitude of 0.3 km s^{-1} . Power spectral analysis of these velocity fluctuations results in a broad peak near five minutes. Phase analysis, performed by taking each pixel as a reference point and computing its cross-spectral with every other pixel in the surrounding area, showed that in regions of high coherence the phases had signatures of propagating waves with speeds of $1\text{--}3 \text{ Mm s}^{-1}$. Most of these waves were propagating outward and aligned well with the direction of the magnetic field.

To confirm this analysis, we performed a phase travel-time analysis (Jefferies, et al. 1994; Finsterle, et al. 2004; McIntosh, et al. 2004) to characterize the propagation characteristics of the wave modes. The data were Fourier filtered in time with a Gaussian filter with a central frequency of 3.5 mHz and a width ($1/e$ folding) of 0.4 mHz . We then formed the cross-correlation map of the filtered time series at the current pixel with nearby pixels sufficient in number to capture all areas of high correlation. The cross-correlation function at each neighboring pixel is a Gabor wavelet that, when fitted, yields information about the group and phase travel times of the disturbance (Finsterle, et al. 2004).

We see from figure 2 (panel A) that the observed oscillations can have very long correlation lengths (the length of the oblong contour of high cross-correlation) and detectable widths. The “island” of high cross-correlation ($CC > 0.5$) also has a distinct direction that follows the apparent trajectory of the propagating wave as seen in the movie. Panel B of figure 3 shows the map of phase travel times in the neighboring pixels relative to the reference pixel; a negative travel time indicates the time taken for the disturbance to travel to the reference pixel and a positive travel time is the time taken from the reference pixel. By using the

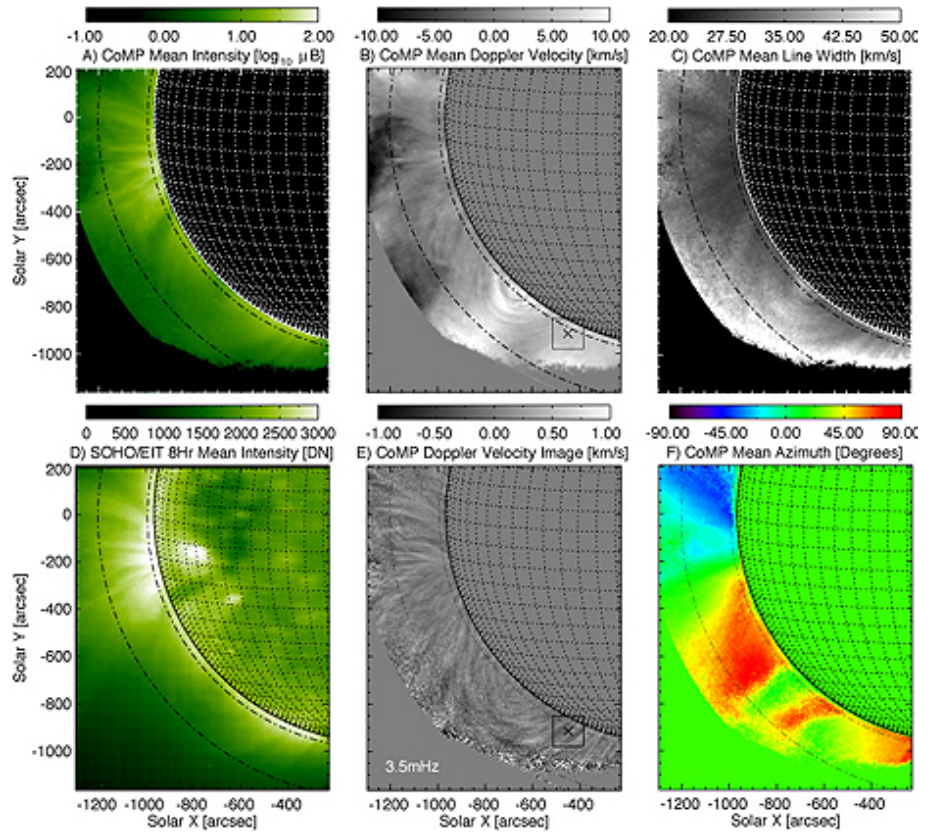


Figure 1: Context for images for the studied observations. From left to right, top to bottom, the CoMP observations of time-averaged intensity (A), Doppler velocity (B), line width (C), plane-of-sky azimuth (F), 3.5 mHz filtered Doppler velocity snapshot (E). In addition, we show the time-averaged SOHO/EIT 195.0 nm image over the same time (D). Each panel shows the location (X) and surrounding square region used for the example of travel-time analysis shown in figure 2. We also show the dot-dashed lines representing distances of 5% and 25% of the solar radius (above the limb) that are used as limits to our analysis.

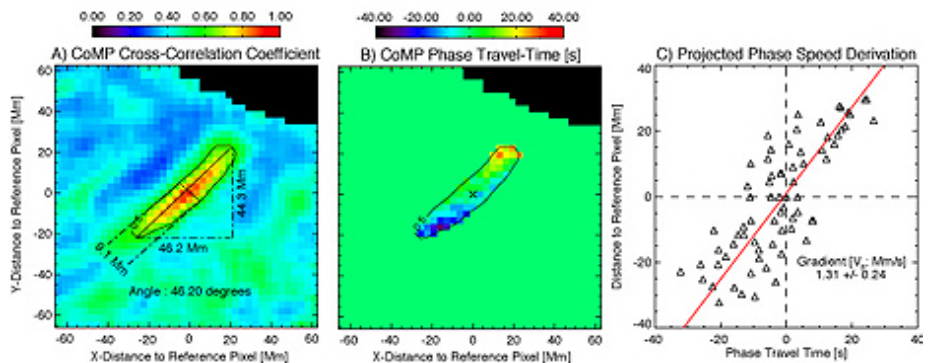


Figure 2: Travel-time analysis of CoMP Doppler velocity measurements for the region shown in figure 1. Panel A shows the map of cross-correlation coefficients in the square (25×25 pixels) region around ($0'', 0''$), the panels B and E of figure 1. The contour shown represents a level of 0.5 in the coherence of the time series and is used to isolate the properties of the oscillations detected. Panel B shows the map of computed phase travel times in the same region (the surrounding pixels are zeroed for clarity). Panel C demonstrates the scatter of phase travel time and distance to the reference pixel; the phase speed of the oscillation in this region is estimated from a least-squares fit.

continued

Observations of Alfvén Waves in the Quiet Solar Corona continued

island of high cross-correlation as a mask, we computed a correlation length of 45 Mm, a width of 9 Mm, a propagation trajectory of $46.2^\circ (\pm 4^\circ)$, and a phase speed of $1.31 (\pm 0.24) \text{ Mm s}^{-1}$ at the reference pixel. This travel-time analysis was repeated successively at all pixels between 1.5 and $1.25 R_{\text{Sun}}$ (dot-dashed lines in figure 1) using each pixel as the reference pixel to extract wave properties at each point (figure 3). Since we also have the plane-of-the-sky azimuth of the coronal field, we can compare it with the direction of wave propagation (figure 4).

We believe that the waves we observe are Alfvén waves because: a) the observed phase speeds ($\approx 2 \text{ Mm s}^{-1}$) are much larger than the sound speed ($\approx 0.22 \text{ Mm s}^{-1}$), therefore, the waves are not slow MA mode waves; b) the spatio-temporal properties of the velocity oscillations and the linear polarization measurements show that these waves propagate along field lines, which would not be the case for fast MA mode waves in the corona; and c) the associated intensity fluctuations are very small. $\text{\textcircled{N}}$

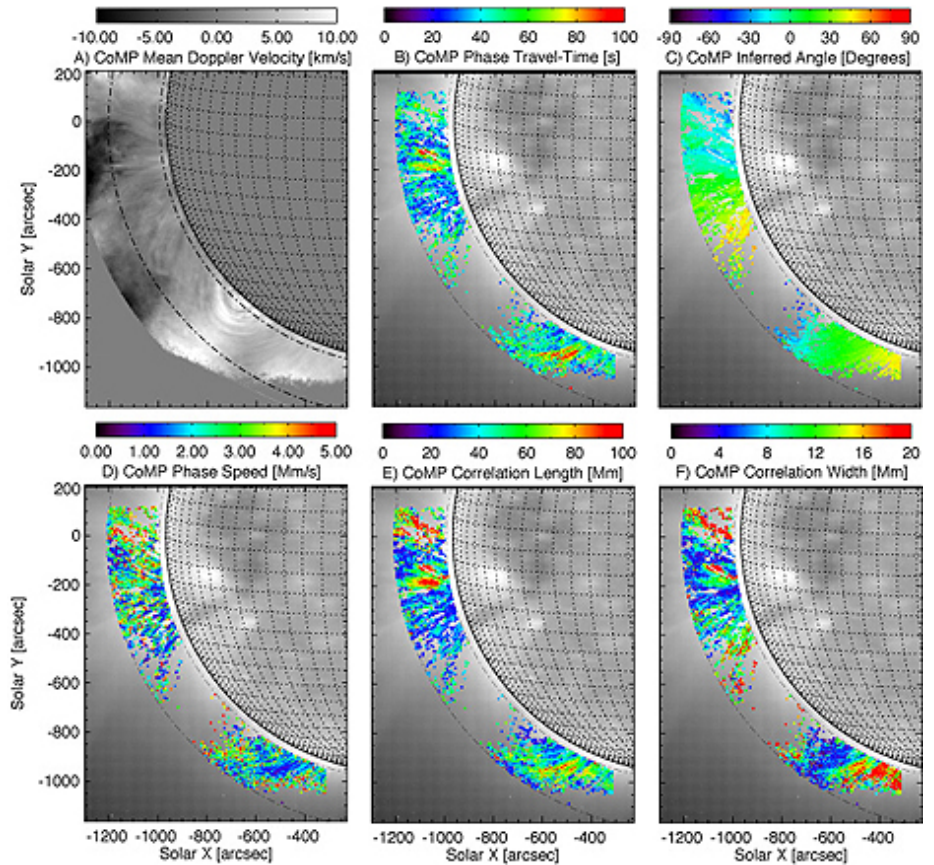


Figure 3: The results of the CoMP travel-time analysis for the $1.05\text{--}1.25 R_{\text{Sun}}$ range superimposed on the SOHO/EIT image shown in figure 1D. Panels B through F show the inferred wave travel time, propagation angle, phase speed, and correlation length and width, respectively. The points shown in each panel represent the analysis of pixels where we have $>99\%$ statistical confidence in the results and the signal-to-noise ratios of the observations are sufficiently high.

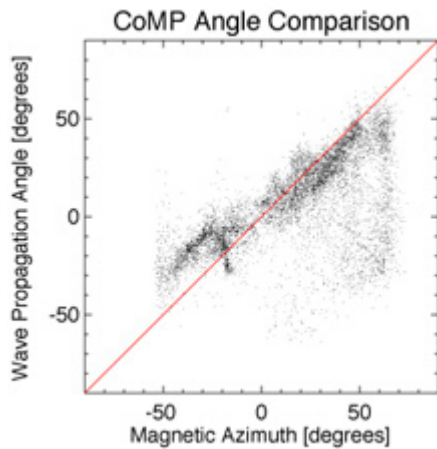


Figure 4: Comparison of measured field azimuth and the inferred wave propagation angle. The values on the abscissa are subject to a 90° ambiguity (van Vleck effect), a fundamental limitation of the information contained in the emission from magnetic dipole coronal lines, in the absence of knowledge of the “atomic alignment.” The abscissa values plotted are those returned from a simple arctangent numerical function. Thus, for example, some of the points near 55° can be justifiably placed at -55° , and vice versa.